# Noninvasive Synchrotron-Based X-ray Raman Scattering Discriminates Carbonaceous Compounds in Ancient and Historical Materials

Pierre Gueriau, Jean-Pascal Rueff, Sylvain Bernard, Josiane Kaddissy, Sarah Goler, Christoph J Sahle, Dimosthenis Sokaras, Roy Wogelius, Phillip Manning, Uwe Bergmann, et al.

## To cite this version:

Pierre Gueriau, Jean-Pascal Rueff, Sylvain Bernard, Josiane Kaddissy, Sarah Goler, et al.. Noninvasive Synchrotron-Based X-ray Raman Scattering Discriminates Carbonaceous Compounds in Ancient and Historical Materials. Analytical Chemistry, 2017, 89 (20), pp.10819-10826. 10.1021/acs.analchem.7b02202 . hal-02128452

## HAL Id: hal-02128452
## https://hal.science/hal-02128452v1

# *In situ* synchrotron-based X-Ray Raman scattering discriminates carbonaceous compounds in ancient and historical materials

Pierre Gueriau[1,2], Jean-Pascal Rueff[2,3], Sylvain Bernard[4], Josiane A. Kaddissy[1], Sarah Goler[5], Christoph Sahle[6], Dimosthenis Sokaras[7], Roy A. Wogelius[8], Philip L. Manning[9], Uwe Bergmann[7]*, Loïc Bertrand[1,2]*

1 IPANEMA, CNRS, Ministère de la culture et de la communication, UVSQ, MNHN, Université Paris-Saclay, 91192 Gif-sur-Yvette, France
2 Synchrotron SOLEIL, BP 48 Saint-Aubin, 91192 Gif-sur-Yvette, France
3 Sorbonne Universités, UPMC Université Paris 06, CNRS, UMR 7614, Laboratoire de Chimie Physique-Matière et Rayonnement, F-75005 Paris, France
4 IMPMC, CNRS UMR 7590, Sorbonne Universités, MNHN, UPMC, IRD UMR 206, 61 rue Buffon, 75005 Paris, France
5 Columbia Nano Initiative, Columbia University, 530 West 120th Street, MC8903 1001 CEPSR, New York, NY 10027, USA
6 ESRF-The European Synchrotron, 71 Avenue des Martyrs, 38000 Grenoble, France
7 Stanford PULSE Institute, SLAC National Accelerator Laboratory, Menlo Park, CA 94025, USA
8 University of Manchester, School of Earth and Environmental Sciences, Williamson Research Centre for Molecular Environmental Science & Interdisciplinary Centre for Ancient Life, M13 9PL, UK
9 Department of Geology and Environmental Geosciences, College of Charleston, 66 George Street, Charleston, SC 29424, USA

## ABSTRACT:

Carbon compounds are ubiquitous and occur in a diversity of chemical forms in many systems including ancient and historic materials ranging from cultural heritage to paleontology. Determining their speciation cannot only provide unique information on their origin, but may also elucidate degradation processes. Synchrotron-based X-ray absorption near-edge structure (XANES) spectroscopy at the carbon K-edge (280–350 eV) is a very powerful method to probe carbon speciation. However, the short penetration depth of soft X-rays imposes stringent constraints on sample type, preparation and analytical environment. A hard X-ray probe such as X-ray Raman Scattering (XRS) can overcome many of these difficulties. Here we report the use of XRS at ~6 keV incident energy to collect carbon K-edge XANES data and probe the speciation of organic carbon in several specimens relevant to cultural heritage and natural history. This methodology enables the measurement to be done in a non-destructive way, in air, and provides information that is not compromised by surface contamination by ensuring that the dominant signal contribution is from the bulk of the probed material. Using the backscattering geometry at large photon momentum transfer maximizes the XRS signal at the given X-ray energy and enhances non-dipole contributions compared to conventional XANES, thereby augmenting the speciation sensitivity. The capabilities and limitations of the technique are discussed. We show that despite its small cross section, for a range of systems the XRS method can provide satisfactory signals at realistic experimental conditions. XRS constitutes a powerful complement to FT-IR, Raman and conventional XANES spectroscopy, overcoming some of the limitations of these techniques.

Ancient and historic materials can be rich in carbon that occurs in a variety of molecular forms. Deciphering the chemical nature of organic compounds within archeological or paleontological specimens lies at the heart of many studies including those dealing with the recognition of past human activities (artworks, tools, textiles, food remains – e.g. Evershed[1]), the reconstruction of palaeo-environments (seeds, plants, pollens, etc. – e.g. Marguerie and Hunot[2]) or the search for the oldest traces of life in rocks (e.g. de Gregorio et al.[3]). Difficulties of characterization and identification of organic compounds is due to their fine scale association with mineral phases and to the alteration that they undergo during ageing.

Invasive methods, based on separative techniques, are used to precisely identify ancient organic molecules in samples where micro-sampling is allowed, however no fine scale spatial information can be resolved from these methods. Fourier transform infrared (FT-IR) spectroscopy, Raman microspectroscopy and time-of-flight secondary ion mass spectrometry (ToF-SIMS) are often used to identify organic compounds and document their chemical nature and the degree of carbon organization[4–6], either through point analyses or imaging. FT-IR and Raman spectroscopies are complementary due to the distinct selection rules. For instance, polar bonds with a significant dipole moment will lead to intense infrared absorption, while usually more polarizable covalent bonds will be intense Raman scatterers. In addition to the intense contribution from fluorescence that often hampers interpretation of the Raman signal in ancient materials, the main limitation of ToF-SIMS, Raman and FT-IR spectroscopies is the shallow information depth. Only the first few micrometers below the surface are probed, thereby exacerbating the contribution of surface contamination or requiring examination of cross sections.

Synchrotron-based X-ray absorption near-edge structure (XANES) spectroscopy at the C K-edge is a very sensitive probe of the local carbon structure and speciation, and has been successfully applied for over two decades to numerous carbonaceous systems[7–9]. Carbon K-edge XANES spectroscopy has been of primary importance to elucidate organic carbon speciation in complex ancient systems[10–12]. Carbon K-edge XANES data can be collected at different spatial resolutions from the tens-of-nanometers to the millimeter scale, by directly measuring transmitted photons (e.g. Jacobsen et al.[8]), emitted electrons (e.g. Boyce et al.[13]) or fluoresced photons (e.g. Alleon et al.[14]). Yet, these approaches require a beam in the soft X-ray range (280–350 eV) that does not penetrate the samples deeper than a few hundred nanometers which imposes very stringent requirements on sample preparation (e.g. FIB ultrathin sectioning, surface ion polishing) and environment (e.g. micro-manipulation, vacuum or low-Z atmosphere).

Inelastic X-ray Raman scattering (XRS[15]) in the hard X-ray range has proven valuable for characterizing the speciation of carbon and other light elements at the bulk scale, or in conditions (e.g. high-pressure cells) not suited for soft X-ray probes[16–21]. The work reported here examines the potential of XRS to elucidate carbon speciation in ancient and historic materials. We show that the method is a practical and powerful complementary probe to discriminate organic compounds in a range of materials from artists' pigments to paleontological macro-remains. We provide numbers to estimate the possibilities and limitations of this hard X-ray speciation probe.

## EXPERIMENTAL SECTION

### XRS based XANES spectroscopy and data processing

XRS relies on the inelastic scattering of incident photons, where the energy transfer of a photon, rather than the absorption of a photon, excites a core electron to a vacant higher-energy molecular orbital. Hence XRS can provide speciation information of light element such as carbon, but with hard X-rays, whereas conventionally such information is obtained by performing XANES in the soft X-ray region. Figure 1 shows the schematics of the XRS setup. A solid sample is illuminated by a tunable, monochromatic X-ray beam with incident energy $E_i$ and momentum $\mathbf{k_i}$. X-rays are then inelastically scattered by the sample at a lower energy $E_f$ with momentum $\mathbf{k_f}$ and detected with a high-resolution analyzer system to determine the energy transfer $E_i - E_f$ and the momentum transfer $\mathbf{q} = \mathbf{k_i} - \mathbf{k_f}$. To obtain a XANES like spectrum with XRS the energy loss Ei – Ef is varied over the same range as the XANES. This can be done by either changing the incident energy $E_i$ at fixed $E_f$, or changing the scattered energy $E_f$ at fixed $E_i$. Most often, the former method is more practical, as it is easier to scan a beamline monochromator than an analyzer.

Most XRS experiments are performed in the 5–10 keV range, due to fundamental and practical considerations (see Sahle et al.[22] and references therein). The low cross-section of XRS requires a very intense monochromatic X-ray source and a large-acceptance analyzer. There is also a spectroscopic benefit of using XRS, because the momentum transfer between the incident and scattered photon, $\mathbf{q}$, takes the role of the polarization vector of the absorbed photon in conventional XANES[23,24]. Unlike the polarization vector that has only a directional value, $\mathbf{q}$ also has a magnitude, and hence non-dipole contributions with additional speciation sensitivity are possible at large enough $\mathbf{q}$. The magnitude of the momentum transfer is given by $q = |\mathbf{k}_i - \mathbf{k}_f| = \sqrt{(k_i^2 + k_f^2 - 2\ k_i\ k_f \cos 2\theta)}$, where $k_{i,f} = 2\pi/\lambda_{i,f}$ is the momentum of the incident/scattered photon of wavelength $\lambda_{i,f,}$ respectively, and $2\theta$ is the scattering angle. Since $k_i$ and $k_f$ have a very similar magnitude (energy loss is small compared to the incident energy), the approximation $q \approx 2k_i \sin\theta$ holds. Significant non-dipole contributions in XRS can occur above the dipole limit given by $q{*}r << 1$, where $r$ is the 1s core radius of the absorbing atom. To determine the best XRS energy, i.e. the scattering angle $2\theta$ and the corresponding $q$ for a given system, compromises that consider several competing parameters have to be found (see also Bergmann et al.[16], Krisch and Sette[18] and Sahle et al.[22]), in particular:

a) X-ray energies should be high enough to achieve the desired penetration into and out of the sample and through any sample enclosures, but low enough to avoid loss in spectral resolution and Bragg analyzer efficiency.

b) XRS scattering angles $2\theta$ too close to $90^o$ should be avoided for horizontal geometries as the XRS signal vanishes due to the linear horizontal polarization of the incident synchrotron beam.

c) XRS energies and momentum transfer $q$ should be chosen that maximize the XRS signal while avoiding too much Compton scattering background (which also depends on $q$).

All XRS measurements presented here were performed at the GALAXIES beamline (SOLEIL synchrotron facility, Saint-Aubin, France). The beamline is equipped with a double crystal Si(1,1,1) monochromator with a beam size of ~30×80 $\mu m^2$ and incident flux of ~$1.5\times10^{13}$ photons/s on the sample[25]. The sample was positioned at an angle of 45° to the incident beam. We used a Rowland geometry XRS spectrometer based on four 100 mm diameter spherically bent Si(n,n,n) Bragg crystals with a radius of curvature of 1 meter. After testing various XRS energies and scattering angles, we found the best compromise of signal to noise, $q$ and space constraints at the GALAXIES beamline to be an XRS scattering angle of $2\theta \sim 137^o$ at a Si(3,3,3) analyzer energy of 5948.85 eV and a Bragg angle of $85.6^o$ (Fig. 1). The overall energy resolution of such configuration was estimated at ~0.8 eV fwhm from the elastic scattering peak width. A silicon drift diode (SDD) detector was placed at a distance of 15.3 cm above the sample on the intersecting Rowland circles. The incident energy range of 6218–6267.5 eV was selected to correspond to an energy transfer of 269.15–318.65 eV. At such energy, the selected XRS scattering angle $2\theta \approx 137^o$ results in $q \approx 5.8$ Å$^{-1}$. The carbon 1s core radius $r$ can be estimated by $a_0/Z$ where $a_0 = 0.529$ Å is the Bohr radius and $Z = 6$ the charge for the carbon nucleus, resulting in $q^*r \approx 0.5$. This value is beyond the dipole limit ($q^*r << 1$) and we observe additional spectral contributions to that in STXM-based XANES due to non dipolar contributions.

Spectra were collected by continuously scanning both the undulator and the monochromator gaps, while monitoring the incident and scattered intensity. A dwell time of 500 ms time per energy step and an energy step size of 0.25 eV were used for each scan. For each sample, several successive spectra were collected on distinct sample pixels, which were later averaged. The spectra were normalized to the incoming beam intensity, measured using a photodiode. Mean spectra were energy-calibrated in order to set the 1s–π* resonance of a graphite reference at 285.4 eV[26]. A pre-edge window of 50 energy points was defined in the 269.15–281.40 eV range below the first 1s–π* contributions at ca. 283 eV. A non-linear fit of this pre-edge signal is performed using a function $y = a/[(x-b)]$[17] and the resulting background contribution is subtracted from the whole spectrum. The relative carbon content in samples of similar carbon chemistry was estimated by comparing integrals of the signal in the 280–291.5 eV range after subtraction of the background, following the procedure in Barré et al.[27] applicable to compounds of similar chemistry at the considered absorption edge for which homothety in the absorption signal results in homothety in the integrated signal. To help comparing the spectra, a normalization is performed by dividing the background-corrected spectrum values by the mean value in a segment of the post-edge spectrum with no significant (or balanced) oscillation. This process was performed through routines using the 'R' statistical environment[28].

### Sample preparation

The samples are described in Table 1. All samples were prepared neat: the graphite, carbon-based pigments and fossil cocoon as powders hold on screw heads; the mammoth samples unprepared, hold on a microscope slide. The screws and microscope slide were then positioned to face the beam.

### Dosimetry

For X-rays in the low and medium-energy range, precise dosimetry is particularly difficult since various interaction processes with different dependences on material properties determine the dose distribution in samples and radiation detectors[29]. Dosimetry was conducted using a calibrated AXUV100 Si photodiode. The diode has a 10×10 mm$^2$ sensitive area with a silicon thickness of 55 µm. Estimates of the surface dose were calculated as $D = n\,h\nu\,\mu/(s\,\rho)$, where $n$ is the photon flux, $h\nu$ the incident photon energy, $\mu$ the attenuation coefficient corresponding to the sum of the atomic photoabsorption and inelastic scattering, $s$ the beam footprint area and $\rho$ the material density, using the experimental parameters used in XRS and STXM-based XANES

## RESULTS AND DISCUSSION

A set of samples was selected in order to test the capabilities of XRS to precisely identify organic compounds in ancient and historic materials (Tab. 1 and Figs. 2 & 3).

### Discrimination of organic compounds.

The denomination "carbon-based pigments" covers a broad family of distinct compounds including graphite and products of combustion or pyrolysis of carbonaceous material: lampblack, acetylene black, gas black, charcoal and bone black. Carbon-based black pigments are notoriously difficult to discriminate[30–33]. In particular, the extremely high absorption of carbon across almost the entire IR–UV range makes absorption spectroscopy difficult and of limited use[31]. The present study illustrates that XRS may help discriminating between these different pigments.

Figure 2A shows the comparison between XRS spectra from three artists' black pigments. Several interesting differences are observed. Assuming that the exact same volume has been measured for the three pigments and that the samples have similar carbon chemistry, the area of the XRS spectrum in the 280–291.5 eV range is directly proportional to the carbon content of the volume sampled[27]. After background subtraction, our data indicate close carbon contents of 64, 61 and 61% for Pigments 1, 2 and 3 respectively (as compared to the graphite area, which corresponds to 100% C). However, the XRS response slightly differs between Pigments 1 and 3, and Pigment 2. Pigments 1 and 3 appear to contain very similar carbon compounds, while after normalization to the carbon content, Pigment 2 exhibits a significantly less intense signal at 285.4 eV and 292.7 eV (attributed to 1s–π* and 1s–σ* electronic transitions in aromatic or olefinic C=C carbons, respectively[34,35]). For highly ordered carbonaceous compounds, the intensities of these absorption features vary with the polarization of the X-ray beam[36,37]. Here, given the likely random orientation of carbonaceous particles within the pigments and given the quite large volume of pigment contributing to the signal, it can be assumed that differences between the spectra shown in Figure 2 do not result from local orientation effects. Because the area of the peak at 285.4 eV is directly related to the aromaticity of the measured compounds in the absence of polarization effects[34,35], it can be concluded that the carbonaceous compounds in Pigment 2 are less graphitic than those composing Pigments 1 and 3. XRS spectral resolution is unfortunately not sufficient to visualize the sharp 1s–σ* exciton at 291.7 eV typical of highly graphitic materials and related to the presence of extensive planar domains of highly conjugated aromatic layers[34,38]. Yet, an additional slight absorption feature is observed at 288.7 eV in the spectrum of Pigment 2. Although it may be attributed to carboxylic functional groups resulting from partial oxidation of the sample[39], this feature more likely corresponds to ''interlayer states'' caused by the presence of stacking defects between the aromatic planes[34,40].

Altogether, the XRS data shown in Figure 2 indicate that the carbon particles of Pigments 1 and 3 are more graphitic than those of Pigment 2. This is totally consistent with the pigments' manufacturing information. In fact, Pigment 2 is identified as "Fine charcoal", while Pigment 1 and 3 are carbon blacks. Carbon blacks are obtained industrially by the burning or pyrolysis of gas or oil, and usually contain a high carbon content[31]. This illustrates the capabilities of XRS-based XANES spectroscopy to discriminate between artists' pigments manufacturing processes.

## Perspectives of spectral interpretation in aged samples.

X-ray absorption spectroscopy is now used on a regular basis in paleontology, as it can provide a wide range of information. Redox-sensitive elements, such as cerium, give clues about the burial and diagenesis environment[41]. Trace metals, such as copper, found in organometallic compounds can reveal critical new paleobiological information (e.g. reconstructing the coloration pattern of fossil birds[42]). Light elements, such as carbon and nitrogen, allow identifying the signature of relict organic molecules, and tracing back their biological origin and/or their alteration through time (e.g. sporopolenin[10] and chitin[43]). The latter have only been performed on extremely thin micro-samples using STXM-based XANES, but could not be applied to fossil macro-remains. The potential of XRS is here demonstrated against two unprepared paleontological samples (Fig. 3): a 49 kyr old mammoth dry skin (see Debruyne et al.[44] for details about the specimen) and a 56 Myr old fossil cocoon, whose morphology suggests affinities with leeches (De Franceschi pers. com.), collected from the Rivecourt site (Oise, France) known to contain abundant animal and plant remains from the Late Paleocene[45].

The XRS-based XANES spectrum of the mammoth dry skin exhibits a small peak at ca. 285.4 eV indicating a low aromaticity of the carbon compounds composing this fossil. A broad and intense feature is observed at 288.7 eV. This feature, complex in shape, is attributed to the overlapping contributions of 1s–π* transitions in amide groups (288.3 eV) and 1s–π* transitions of carboxyl groups (288.7[46]). Absence of significant signal at 290.3 and 300 eV points to the absence of carbonate minerals, which was independently confirmed by observation of a typical amorphous powder XRD pattern (*data not shown*). A very similar spectrum was reported on a modern collagenous rat-tail tendon[47], which is another evidence of the very good chemical preservation of the organic compounds composing this ancient mammoth dry skin.

Although both samples show a main absorption at 288.7 eV (likely attributed to joint contributions of amide and carboxyl carbons), the XRS-based XANES spectrum of the cocoon significantly differs from that of the mammoth dry skin. The small peak at 285.4 eV, attributed to the presence of aromatic and/or olefin carbons, appears broader than in the mammoth dry skin. This unusual width may be related to the presence of graphitic domains disseminated within a globally turbostratic matrix[34]. In addition, the XRS-based XANES spectrum of the paleontological cocoon exhibits a weak shoulder at 287.2 eV. The STXM-based XANES spectrum collected on an ultrathin section of the same cocoon sample (CLS SM beamline 10ID-1[48]) exhibits the same absorption features, but the peak at 285.4 eV is more intense and the feature at 287.2 eV is more individualized. These differences are probably attributable to the lower energy resolution of XRS compared to that of STXM, but may also result from additional non-dipole contributions that can be seen using XRS. Clear absence of peaks attributable to carbonates is in agreement with additional powder XRD measurements that only detect limited presence of quartz and calcite as contributing minerals (*data not shown*).

A spectral decomposition of the XANES data was performed. Reduction of the spectra to a limited number of contributing features can compensate the moderate energy resolution of the collected XRS data. Features from diagnostic transitions were modeled as Gaussian distributions, as described for amino acids[49] (Fig. 4; see Tab. S-1 for center, fwhm, intensity and assignment of the Gaussian peaks). The quality of the spectra proved sufficient to yield satisfactory spectral decomposition of the XRS data with barely structured residual features. The decomposition clearly confirms the presence of a contribution at ca. 287.2 eV in the fossil cocoon, while it is very significantly weaker in the mammoth sample (Fig. 4; Tab. S-1). Indeed, decomposition without taking into account this contribution results in a structured residue (see "residue 2" in Fig. 4). This peak is likely attributed to 1s–σ* transitions from bonds formed between carbon and heteroatoms such as sulfur (1s–σ* C–S). Leech cocoon membranes are known to be very rich in sulfur owing to the cysteine residues that contribute to their mechanical and physico-chemical stability by forming intra- and/or intermolecular disulphide cross-linking[50]. This would strongly support leech affinities for the Rivecourt cocoon. Another spectral feature appears at ca. 292.4 eV, that could be related to C–C 1s–σ* contributions (293–297 eV). However, at this energy slightly above the carbon ionization energy, attribution to multiple scattering cannot be excluded.

## Advantages and limitations of XRS-based XANES

In the conditions proposed here for XRS based XANES, the attenuation length (1/e) of the ~6 keV X-ray beam is ~0.5 mm in organic compounds, exceeding the value for fluorescence detected XANES (~100 nm) by more than three orders of magnitude. XRS-based XANES is therefore (1) far less sensitive to surface contamination than STXM- or PEEM-based XANES, and (2) provides bulk information over a far greater information depth. This largely facilitates sample preparation compared to ultramicrotomy or focused ion beam micromachining usually employed in STXM- or PEEM-based XANES. The sample surface should just be of moderate roughness at the sub-mm length scale. Potential spectral contribution from surface soiling and contaminant deposition is decreased to a negligible extent. In addition, this increase in information volume is particularly interesting for graphitic powders such as our carbon black artists' pigments. Collected spectra will reflect average features from the graphitic powder rather than a measure of locally oriented sheets in turbostratic graphite (see Fig. 2B for graphite XRS spectra). Moreover, 1 cm of air will absorb less than 3% of the intensity of a 6-keV X-ray beam, and all our experiments were performed with the sample in air. The acceptance of the detection system, focused on the sample, and the far greater carbon quantities in the sample than in air therefore contribute to vastly facilitated sample preparation and handling. The XRS high-$q$ geometry ($q \sim 5.8$ Å$^{-1}$, i.e. significantly above the dipole limit) allows non-dipole contributions. In our measured spectra, we observe an enhancement of the C=C 1s–π* resonance as well as other resonances (indicated by arrows in Fig. 2B) as compared to low-$q$ XRS spectra. These effects were first reported on oriented graphite by Schülke et al.[23].

The low intensity of the XRS signal and relatively large background mainly from Compton scattering are probably the most severe limitations of this technique. It was therefore important to optimize the experimental geometry for best signal to noise ratio. Even after optimization, using an incoming flux of $1.5\times10^{13}$ ph/s, we obtained a carbon signal of $10^2$–$10^3$ ph/s, on a background of a few $10^2$ ph/s depending on carbon concentration and matrix composition. The practical application of XRS to ancient materials is therefore restricted to samples that are relatively high in carbon concentration (at least a few percent), and matrices that are not too absorbing for X-rays at 5–10 keV in order to ensure a sufficiently large scattering volume. The spatial resolution is comparable to that obtained in fluorescence-detection XANES but far lower than in STXM-based C-XANES (but with much easier sample preparation and handling) to maintain a high count while decreasing the surface dose.

As a very intense X-ray beam and/or a large acceptance XRS spectrometer are required to compensate the low efficiency of the X-ray Raman process, specific care needs to be taken to mitigate and monitor the possible formation of radiation-induced sample damage. Mitigation and monitoring of radiation-induced side effects is essential for ancient and historic materials[51]. The surface dose rate corresponding to our experimental conditions is 12 times greater in STXM than in XRS in chitin, and 1.8 times lower in STXM than in XRS in calcite, as calcite has a greater absorbance in the hard X-ray (Tab. 2). However, as the XRS phenomenon has a much lower cross section and as additional signal loss originates from the analyzer optics, it requires much longer data acquisition (for the data shown in Fig. 2 the acquisition time was 50 longer than for STXM). The integrated surface doses are therefore typically 1 to 2 orders of magnitude greater in XRS than in STXM. Specific attention should therefore be paid to the possibility of radiation-induced side effects, and acquisition at a limited number of energies should be favored rather than acquisition of full XANES or EXAFS spectra. Nevertheless, the XRS spectra presented herein do not seem to have been affected by radiation-side effects. Indeed, no signal change was observed during data collection on the ancient samples. Exposure of the fossil cocoon to an unrealistically high dose results in a very different spectrum than the one discussed (Fig. S–1). More generally, from observation of changes in the XRS signal, we observed that ancient and historic systems were more resistant to radiation damage than our model carbonaceous systems, probably owing to their "physico-chemical resilience" after long-term aging. Only on recent resin and standard samples did we observe decreasing signal intensity between successive spectra, i.e. over irradiation duration below 100 s.

## CONCLUSION

This work shows that XRS-based XANES is a powerful and practical method to study the speciation of carbon-based compounds in ancient and historic materials from the arts, archaeology and paleontology, and as such, appears highly complementary to well established analytical spectroscopic methods[52,53]. This hard X-ray (5–10 keV) surrogate of XANES could be performed directly with minimal preparation on samples owing to its bulk sensitivity, in the millimeter length scale. Spectral quality is sufficient to allow fine interpretation of spectra. Non-dipole contributions to the XRS based XANES spectra can enhance the speciation in a fingerprinting sense, although their interpretation might sometimes be challenging[54]. Given the collected spectra quality, and the fact that one order of magnitude more efficient XRS spectrometers exist[55,56], one can envision that this method be effectively applied to a wide range of ancient and historic materials, even at submicrometric scales. Beyond carbon, XRS-based XANES can also probe the speciation of many light elements that usually pose similar significant analytical difficulties, such as oxygen, nitrogen and sulfur. There is no doubt that optimized XRS-based XANES spectroscopy can provide invaluable information regarding the speciation of light elements in many heterogeneous materials encountered in materials, Life, Earth and environmental sciences.

## AUTHOR INFORMATION

### Author Contributions

UB and LB defined the original concept and the experiments. LB, UB and PG coordinated and wrote the manuscript with contributions from all authors. All authors contributed to data interpretation. All authors have given approval to the final version of the manuscript.

### Associated content

**Supporting information.**
STXM-based XANES data collection and processing. Details about the experimental setup and data processing.
Table S-1: Center, fwhm, intensity and assignment of the peaks from the Gaussian decomposition of the mammoth and fossil cocoon spectra.
Figure S-1: Background-corrected normalized X-ray Raman spectra of the 56-Myr old fossil cocoons from the Rivecourt site using XRS, STXM, and STXM after high dose.

### Notes

The authors declare no competing financial interest.

## ACKNOWLEDGMENT

We thank Jérémy Hénin (IPANEMA) for support on sample preparation. Guillaume Billet (MNHN) provided the loan and catalogue number of the mammoth sample, and Gaël de Plöeg (CPIE) and Dario De Franceschi (MNHN) of the fossil cocoons. We acknowledge SOLEIL for provision of synchrotron radiation facilities (proposal no. 99160123). Portions of this research were carried out at the Stanford Synchrotron Radiation Lightsource (SSRL), a user facility of the U.S. Department of Energy (DOE), Office of Basic Energy Sciences. STXM-based X-ray absorption spectroscopy data were acquired at beamline 10ID-1 at the CLS, which is supported by the NSERC, the CIHR, the NRC and the University of Saskatchewan. Special thanks go to Jian Wang and Jay Dynes for their expert support, and to Karen Trentelman (Getty Conservation Institute, Los Angeles, CA) for advice on the manuscript. UB and LB acknowledge support from LabEx PATRIMA / Fondation des Sciences du Patrimoine and the France–Stanford Center for Interdisciplinary Studies Program. SB acknowledges support from the ERC project PaleoNanoLife (P.I.: F. Robert). LB acknowledges support by the ANR project EquipEx PATRIMEX and DIM Matériaux anciens et patrimoniaux (Région Île-de-France). JK acknowledges support from the European Commission within the Horizon2020 framework program (IPERION CH, G.A. No. 654028) and the RADDAM project of the LabEx PATRIMA.

## REFERENCES

(1) Evershed, R. P. *Archaeometry* **2008**, *50*, 895–924.

(2) Marguerie, D.; Hunot, J.-Y. *Journal of archaeological science* **2007**, *34*, 1417–1433.

(3) De Gregorio, B. T.; Sharp, T. G.; Flynn, G. J.; Wirick, S.; Hervig, R. L. *Geology* **2009**, *37*, 631–634.

(4) Sandford, S. A.; Aléon, J.; Alexander, C. M.; Araki, T.; Bajt, S.; Baratta, G. A.; Borg, J.; Bradley, J. P.; Brownlee, D. E.; Brucato, J. R.; *et al. Science* **2006**, *314*, 1720–1724.

(5) Mazel, V.; Richardin, P.; Debois, D.; Touboul, D.; Cotte, M.; Brunelle, A.; Walter, P.; Laprévote, O. *Analytical Chemistry* **2007**, *79*, 9253–9260.

(6) Casadio, F.; Daher, C.; Bellot-Gurlet, L. *Topics in Current Chemistry* **2016**, *374*, 1–51.

(7) Stohr, J. *NEXAFS spectroscopy*; Springer-Verlag Berlin, 1992; Vol. 25.

(8) Jacobsen, C.; Wirick, S.; Flynn, G.; Zimba, C. *Journal of Microscopy* **2000**, *197*, 173–184.

(9) Bluhm, H.; Andersson, K.; Araki, T.; Benzerara, K.; Brown, G. E.; Dynes, J. J.; Ghosal, S.; Gilles, M. K.; Hansen, H.-C.; Hemminger, J.; *et al. Journal of Electron Spectroscopy and Related Phenomena* **2006**, *150*, 86–104.

(10) Bernard, S.; Benzerara, K.; Beyssac, O.; Brown, G.; Stamm, L. G.; Duringer, P. *Review of Palaeobotany and Palynology* **2009**, *156*, 248–261.

(11) Cosmidis, J.; Benzerara, K.; Gheerbrant, E.; Esteve, I.; Bouya, B.; Amaghzaz, M. *Geobiology* **2013**, *11*, 139–153.

(12) Alleon, J.; Bernard, S.; Le Guillou, C.; Marin-Carbonne, J.; Pont, S.; Beyssac, O.; McKee- gan, K. D.; Robert, F. *Nature Communications* **2016**, *7*, 11977. *(2016a)*

(13) Boyce, C. K.; Cody, G. D.; Feser, M.; Jacobsen, C.; Knoll, A.; Wirick, S. *Geology* **2002**, *30*, 1039–1042.

(14) Alleon, J.; Bernard, S.; Le Guillou, C.; Daval, D.; Skouri-Panet, F.; Pont, S.; Delbes, L.; Robert, F. *Chemical Geology* **2016**, *437*, 98–108. *(2016b)*

(15) Suzuki, T. *Journal of the Physical Society of Japan* **1967**, *22*, 1139–1150.

(16) Bergmann, U.; Glatzel, P.; Cramer, S. P. *Microchemical Journal* **2002**, *71*, 221–230.

(17) Bergmann, U.; Groenzin, H.; Mullins, O. C.; Glatzel, P.; Fetzer, J.; Cramer, S. *Chemical Physics Letters* **2003**, *369*, 184–191.

(18) Krisch, M.; Sette, F. *Surface Review and Letters* **2002**, *9*, 969–976.

(19) Mao, W. L.; Mao, H.-K.; Eng, P. J.; Trainor, T. P.; Newville, M.; Kao, C.-C.; Heinz, D. L.; Shu, J.; Meng, Y.; Hemley, R. J. *Science* **2003**, *302*, 425–427.

(20) Wernet, P.; Nordlund, D.; Bergmann, U.; Cavalleri, M.; Odelius, M.; Ogasawara, H.; Näslund, L.-Å.; Hirsch, T.; Ojamäe, L.; Glatzel, P.; *et al. Science* **2004**, *304*, 995–999.

(21) Rueff, J.-P.; Shukla, A.; *Reviews of Modern Physics* **2010**, *82*, 847.

(22) Sahle, C. J.; Mirone, A.; Niskanen, J.; Inkinen, J.; Krisch, M.; Huotari, S. *Journal of Synchrotron Radiation* **2015**, *22*, 400–409.

(23) Schülke, W.; Bonse, U.; Nagasawa, H.; Kaprolat, A.; Berthold, A. *Physical Review B* **1988**, *38*, 2112–2123.

(24) Krisch, M.; Sette, F.; Masciovecchio, C.; Verbeni, R. *Physical Review Letters* **1997**, *78*, 2843.

(25) Rueff, J.-P.; Ablett, J.; Céolin, D.; Prieur, D.; Moreno, T.; Balédent, V.; Lassalle-Kaiser, B.; Rault, J.; Simon, M.; Shukla, A. *Journal of Synchrotron Radiation* **2015**, *22*, 175–179.

(26) Bergmann, U.; Mullins, O. C. In *Asphaltenes, heavy oils, and petroleomics*; Mullins, O. C., Sheu, E. Y., Hammami, A., Marshall, A. G., Eds.; Springer Science & Business Media, 2007; pp 139–155.

(27) Barré, P.; Plante, A. F.; Cécillon, L.; Lutfalla, S.; Baudin, F.; Bernard, S.; Christensen, B. T.; Eglin, T.; Fernandez, J. M.; Houot, S.; *et al. Biogeochemistry* **2016**, *130*, 1–12.

(28) R Development Core Team, *R Foundation for Statistical Computing, Vienna, Austria* **2011**.

(29) Kron, T.; Duggan, L.; Smith, T.; Rosenfeld, A.; Butson, M.; Kaplan, G.; Howlett, S.; Hyodo, K. *Physics in Medicine and Biology* **1998**, *43*, 3235–3259.

(30) Winter, J. *Studies in Conservation* **1983**, *28*, 49–66.

(31) Winter, J.; FitzHugh, E. W. In *Artists' pigments: a handbook of their history and characteristics*; Berrie, B. H., Ed.; Archetype, London, 2007; Vol. 4; pp 1–37.

(32) Tomasini, E. P.; Halac, E. B.; Reinoso, M.; Di Liscia, E. J.; Maier, M. S. *Journal of Raman Spectroscopy* **2012**, *43*, 1671–1675.

(33) Cersoy, S.; Martinetto, P.; Bordet, P.; Hodeau, J. L.; Van Elslande, E.; Walter, P. *Journal of Applied Crystallography* **2016**, *49*, 585–593.

(34) Bernard, S.; Beyssac, O.; Benzerara, K.; Findling, N.; Tzvetkov, G.; Brown, G. *Carbon* **2010**, *48*, 2506–2516.

(35) Bernard, S.; Benzerara, K.; Beyssac, O.; Balan, E.; Brown Jr., G. E.; *Heliyon* **2015**, *1*, e00034.

(36) Rosenberg, R. A.; Love, P. J.; Rehn, V.; *Physical Review B* **1986**, *33*, 4034–4037.

(37) Brandes, J. A.; Cody, G. D.; Rumble, D.; Haberstoh, P.: Wirick, S.; Gelinas, Y. *Carbon* **2008**, *46*, 1424–1434.

(38) Ahuja, R.; Brühwiler, P. A.; Wills, J. M.; Johansson, B.; Martensson, N.; Eriksson, O. *Physical Review B* **1996**, *54*, 14396–14404.

(39) Atamny, F.; Blöcker, J.; Henschke, B.; Schlögl, R.; Schedel-Niedrig, T.; Keil, M.; Bradshaw, A.M. *The Journal of Physical Chemistry* **1992**, *96*, 4522–4526.

(40) Fisher, D. A.; Wentzcovitch, R. M.; Carr, R. G.; Continenza, A.: Freeman, A. J. *Physical Review B* **1991,** *44*, 1427–1429.

(41) Gueriau, P.; Mocuta, C.; Bertand, L. Analytical Chemistry **2015**, *87*, 8827–8836.

(42) Wogelius, R. A.; Manning, P. L.; Barden, H. E.; Edwards, N. P.; Webb, S. M.; Sellers, W. I.; Taylor, K. G.; Larson, P. L.; Dodson, P.; You, H.; et al. Science **2011**, *333*, 1622–1626.

(43) Cody, G. D.; Gupta, N. S.; Briggs, D. E. G.; Kilcoyne, A. L. D.; Summons, R. E.; Kenig, F.; Plotnick, R. E.; Scott, A. C. Geology 2011, 39, 255–258.

(44) Debruyne, R.; Barriel, V.; Tassy, P. *Molecular Phylogenetics and Evolution* **2003**, *26*, 421–434.

(45) Smith, T.; Quesnel, F.; De Plöeg, G.; De Franceschi, D.; Métais, G.; De Bast, E.; Solé, F.; Folie, A.; Boura, A.; Claude, J.; et al. *PloS ONE* **2014**, *9*, e86229.

(46) Solomon, D.; Lehmann, J.; Kinyangi, J.; Liang, B.; Heymann, K.; Dathe, L.; Hanley, K.; Wirick, S.; Jacobsen, C. *Soil Science Society of America Journal* **2009**, *73*, 1817–1830.

(47) Lam, R. S.; Metzler, R. A.; Gilbert, P. U.; Beniash, E. *ACS chemical biology* **2012**, *7*, 476–480.

(48) Kaznatcheev, K.; Karunakaran, C.; Lanke, U.; Urquhart, S.; Obst, M.; Hitchcock, A. *Nuclear Instruments and Methods in Physics Research Section A: Accelerators, Spectrometers, Detectors and Associated Equipment* **2007**, *582*, 96–99.

(49) Zubavichus, Y.; Shaporenko, A.; Grunze, M.; Zharnikov, M. *The Journal of Physical Chemistry A* **2005**, *109*, 6998–7000.

(50) Mason, T. A.; McIlroy, P. J.; Shain, D. H. *FEBS Letters* **2004**, *561*, 167–172.

(51) Bertrand, L.; Schöeder, S.; Anglos, D.; Breese, M. B.; Janssens, K.; Moini, M.; Simon, A. *Trends in Analytical Chemistry* **2015**, *66*, 128–145.

(52) Bertrand, L.; Bernard, S.; Marone, F.; Thoury, M.; Reiche, I.; Gourrier, A.; Sciau, P.; Bergmann, U. *Topics in Current Chemistry* **2016**, *374*, 1–39.

(53) Gueriau, P.; Bernard, S.; Bertrand, L. *Elements* **2016**, *12*, 45–50.

(54) Feng, Y.; Seidler, G.; Cross, J.; Macrander, A.; Rehr, J. *Physical Review B* **2004**, *69*, 125402.

(55) Sokaras, D.; Nordlund, D.; Weng, T.-C.; Alonso Mori, R.; Velikov, P.; Wenger, D.; Garachtchenko, A.; George, M.; Borzenets, V.; Johnson, B.; *et al. Review of Scientific Instruments* **2012**, *83*, 043112.

(56) Huotari, S.; Sahle, C. J.; Henriquet, C.; Al-Zein, A.; Martel, K.; Simonelli, L.; Verbeni, R.; Gonzalez, H.; Lagier, M.-C.; Ponchut, C.; *et al. Journal of Synchrotron Radiation* **2017**, *24*, 521–530.

**Table 1.** Description of the set of ancient and historic samples used to develop the proposed analytical methodology.

| Sample | Description | Origin | Inv. no. |
|---|---|---|---|
| Pigment 1 | Carbon black – “Carbon black”, from no. 6 type oil | Rockwood Inc. | LB-1011 |
| Pigment 2 | Charcoal – “Fine charcoal”, from beechwood 500°C | Kremer Inc. | 47800 |
| Pigment 3 | Lampblack – “Furnace Black, Lamp Black Slow drier, light-weight powder, from acetylene” | Kremer Inc. | 47250 |
| Pure graphite | Ultra F’ purity graphite T.M.I. 5 ppm Ultra Carbon. Powder 200 mesh. Batch: 169-717 | Alfa Johnson Matthey Gmbh | 291-955-3 |
| Rivecourt cocoon | 56-Myr old fossil cocoon | Rivecourt (France)<br>Material taken to the MNHN for study; will later be housed at musée Vivenel (Compiègne, France) | RIV.PPA 1 (field number) |
| Mammoth | Fragment from the dry skin of a 49,000 yr-old fossil mammoth | Lyakhov island (Siberia)<br>MNHN palaeontological collections | MNHN.F. MAQ 287 |

**Table 2.** Irradiation surface dose rates and integrated surface doses in XRS and STXM based C-XANES calculated from realistic experimental parameters for pure chitin and calcite.

| Experiment | STXM[2] | | XRS[3] | |
|---|---|---|---|---|
| Compound[1] | Surface dose rate (MGy/s)[4] | Integrated surface dose (MGy) | Surface dose rate (MGy/s) | Integrated surface dose (MGy) |
| Chitin | 91 ± 18 | 64 ± 13 | 7.3 ± 1.5 | $7.2\times10^2$<br>$\pm 1.4\times10^2$ |
| Calcite | 39 ± 8 | 28 ± 6 | 71 ± 14 | $7.0\times10^3$<br>$\pm 1.4\times10^3$ |

[1] Chitin and calcite are approximated as $C_8H_{13}O_5N$ (d=1.37) and $CaCO_3$ (d=2.70), respectively.

[2] Experimental conditions considered for STXM C-XANES experiments: E=300 eV, round beam diameter 20 nm, flux $1\times10^6$ ph/s on sample, 700 energy steps of 10 ms each.

[3] Experimental conditions considered for XRS C-XANES experiments: E=6 keV, beam area $30\times80\times\sqrt{2}$ $\mu m^2$, flux $1.5\times10^{13}$ ph/s on sample, 135 s including dead time per spectrum.

[4] The error on the beam size and flux leads to an overall error in the doses estimated to ±20%.

**Figure 1.** Top view of the schematics of the experimental setup of the XRS setup. The detector (not shown) is placed at a distance of 15.3 cm above the sample in a Rowland circle geometry using spherically bent Si(3,3,3) analyzers at a Bragg angle of 85.6° and a photon energy of 5948.85 eV. The XRS scattering angle was set to 137° to maximize the XRS signal to noise at this photon energy.

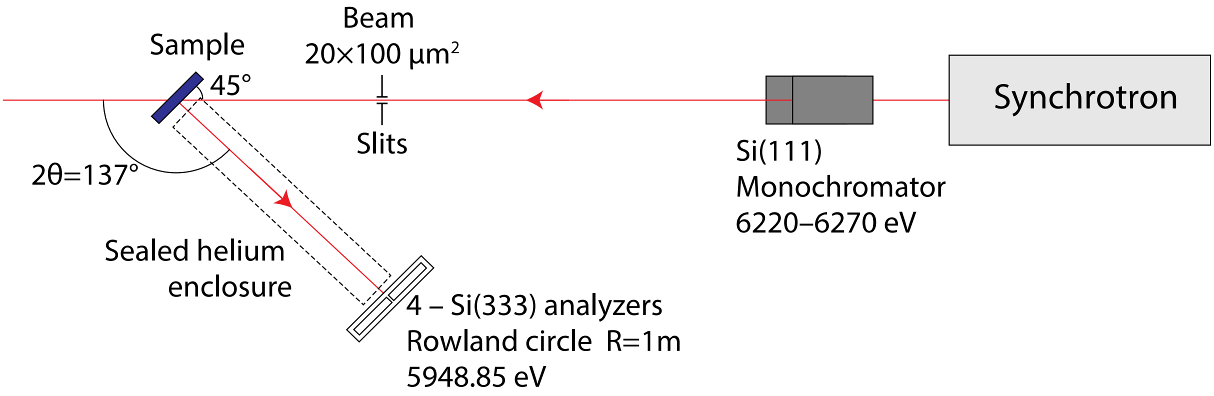

**Figure 2:** Background-corrected normalized X-ray Raman spectra of carbon-based pigments. From top to bottom: (A) three artists' black pigments; (B) Pure graphite at high-*q* compared to the low-*q* spectrum from Bergmann et al.[16]. Arrows indicate enhancements of resonances due to our high-*q* geometry, as compared to a low-*q* XRS spectrum

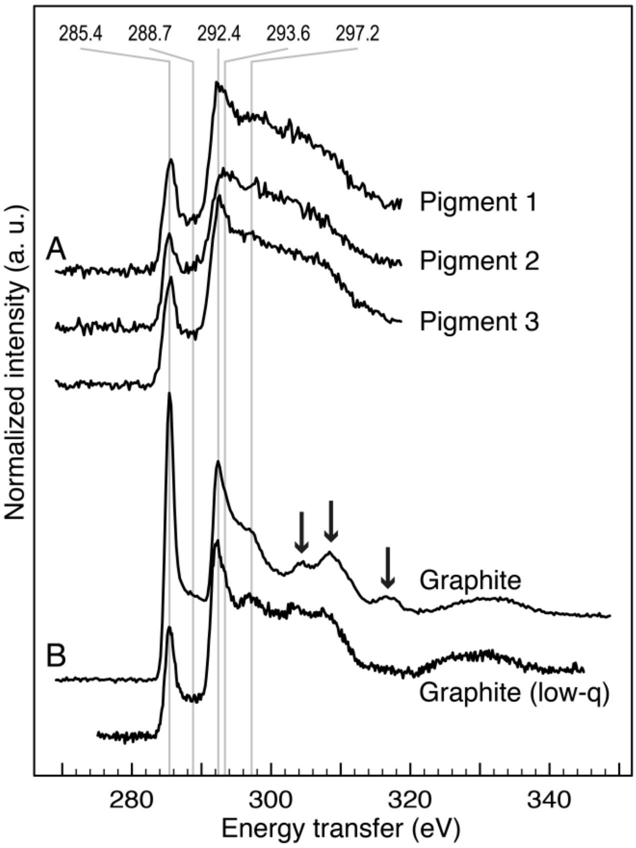

**Figure 3:** Background-corrected normalized X-ray Raman spectra of paleontological samples. From top to bottom: (A) Fragment of dry skin from a 49,000-yr old mammoth from Siberia; (B) 56-Myr old fossil cocoon from the Rivecourt site, XRS and STXM spectra.

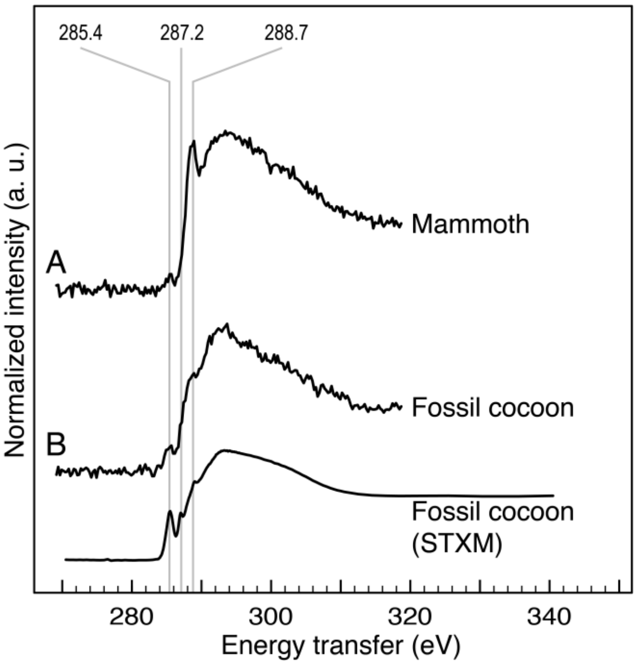

**Figure 4:** Decomposition in 7 Gaussian contributions of the XRS spectra and corresponding fit residues (“residue 1”) from the paleontological cocoon (A) and the fragment of dry skin from the 49,000-yr old mammoth (B). “Residue 2” is calculated from a fit omitting the second Gaussian feature attributed to the 1s–σ* C–S transition. Note the significant remaining contribution in Residue 2 for the paleontological cocoon. For clarity, the residues are shifted down along the vertical axis. Refer to Table S-1 for details about the center, fwhm, intensity and assignment of the peaks.

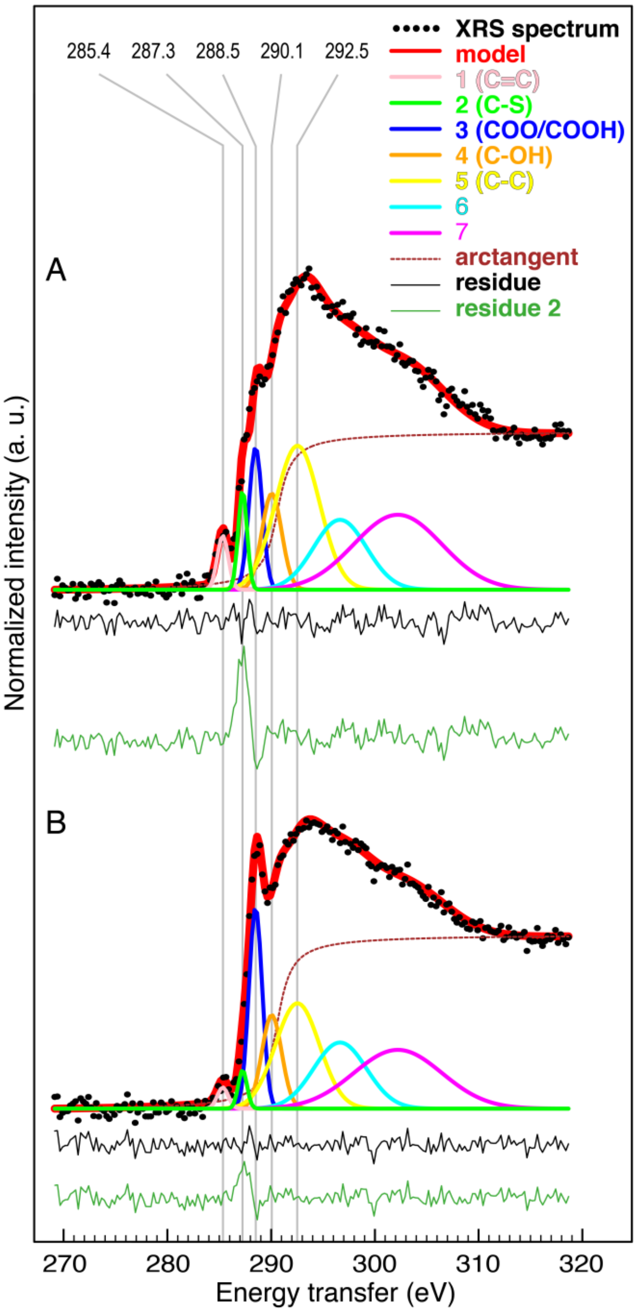

"for TOC only"

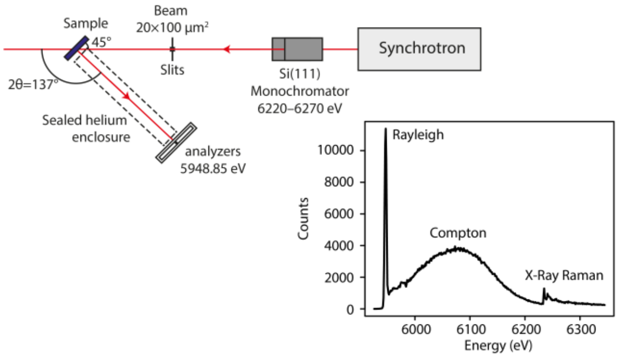
Sample
45°
2θ=137°
Beam
20×100 μm²
Slits
Si(111)
Monochromator
6220–6270 eV
Synchrotron
Sealed helium
enclosure
analyzers
5948.85 eV
Rayleigh
Compton
X-Ray Raman
Counts
0
2000
4000
6000
8000
10000
6000
6100
6200
6300
Energy (eV)